Spin−Orbit Mixing and Nephelauxetic Effects in the Electronic Spectra of Nickel(II)-Encapsulating Complexes Involving Nitrogen and Sulfur Donors

Robert Stranger,*,† Katie L. McMahon,‡ Lawrence R. Gahan,§ James I. Bruce,§ and Trevor W. Hambley||

Department of Chemistry, Faculties, The Australian National University, Canberra, ACT 0200, Australia, Centre for Magnetic Resonance and Department of Chemistry, The University of Queensland, Brisbane, QLD 4072, Australia, and School of Chemistry, The University of Sydney, Sydney, NSW 2006, Australia

Received December 4, 1996[⊗]

A study of spin−orbit mixing and nephelauxetic effects in the electronic spectra of nickel(II)-encapsulating complexes involving mixed nitrogen and sulfur donors is reported. As the number of sulfur donors is systematically varied through the series $[Ni(N_{6-x}S_x)]^{2+}$ ($x = 0-6$), the spin-forbidden $^3A_{2g} \rightarrow {}^1E_g$ and $^3A_{2g} \rightarrow {}^1A_{1g}$ transitions undergo a considerable reduction in energy whereas the spin-allowed transitions are relatively unchanged. The $[Ni(diAMN_6sar)]^{2+}$ and $[Ni(AMN_5Ssar)]^{2+}$ complexes exhibit an unusual band shape for the $^3A_{2g} \rightarrow {}^3T_{2g}$ transition which is shown to arise from spin−orbit mixing of the E spin−orbit levels associated with the ^1E_g and $^3T_{2g}$ states. A significant differential nephelauxetic effect also arises from the covalency differences between the t_{2g} and e_g orbitals with the result that no single set of Racah *B* and *C* interelectron repulsion parameters adequately fit the observed spectra. Using a differential covalency ligand-field model, the spectral transitions are successfully reproduced with three independent variables corresponding to 10*Dq* and the covalency parameters f_t and f_e, associated with the t_{2g} and e_g orbitals, respectively. The small decrease in f_t from unity is largely attributed to central-field covalency effects whereas the dramatic reduction in f_e with increasing number of sulfur donors is a direct consequence of the increased metal−ligand covalency associated with the sulfur donors. Covalency differences between the t_{2g} and e_g orbitals also result in larger 10*Dq* values than those obtained simply from the energy of the $^3A_{2g} \rightarrow {}^3T_{2g}$ spin-allowed transition.

Introduction

In earlier reports[1] we have examined the electronic spectra of the octahedral nickel(II) complexes $[Ni([9]aneN_3)_2]^{2+}$ and $[Ni(AMN_4S_2sar)]^{2+}$ from two very different perspectives. In $[Ni([9]aneN_3)_2]^{2+}$, we were largely concerned with the role of spin−orbit coupling in influencing the band shape of the lowest energy spin-allowed transition. This complex, like a number of other six-coordinate Ni(II) complexes involving nitrogen donors such as $[Ni(en)_3]^{2+}$, $[Ni(bipy)_3]^{2+}$, and $[Ni(phen)_3]^{2+}$, exhibits an unusual double-humped band shape associated with the spin-allowed $^3A_{2g} \rightarrow {}^3T_{2g}$ transition.[2] In the past, this feature has been attributed to either (i) low-symmetry splitting of the $^3T_{2g}$ state, (ii) spin−orbit splitting of the $^3T_{2g}$ state, or (iii) mixing of the ^1E_g and $^3T_{2g}$ states through spin−orbit coupling. In the absence of unambiguous assignments for the $^3T_{2g}$ and ^1E_g states, the double-humped nature of the $^3A_{2g} \rightarrow {}^3T_{2g}$ transition has led to unrealistically high values for the Racah *B* interelectron repulsion parameter as well as erroneous values of 10*Dq*. Our study[1a] of the $^3A_{2g} \rightarrow {}^3T_{2g}$ transition in $[Ni([9]aneN_3)_2]^{2+}$, however, clearly showed that the anomalous band shape was primarily the result of spin−orbit mixing between the ^1E_g and $^3T_{2g}$ states such that the intensity of the spin-forbidden $^3A_{2g} \rightarrow {}^1E_g$ transition was significantly enhanced, leading to the double-humped band feature. From an analysis of the $^3A_{2g} \rightarrow {}^3T_{2g}$ band envelope, we were able to ascertain the contribution of the spin-forbidden $^3A_{2g} \rightarrow {}^1E_g$ transition to the overall band shape and thus derive sensible values of the ligand-field parameters for this complex.

In our study[1b] of the second complex, $[Ni(AMN_4S_2sar)]^{2+}$, we were interested in rationalizing the rather poor agreement between the observed and calculated energies of the spin-forbidden $^3A_{2g} \rightarrow {}^1E_g$ and $^3A_{2g} \rightarrow {}^1A_{1g}$ transitions when using ligand-field parameters optimized for the observed spin-allowed bands. Our analysis revealed the presence of a substantial differential nephelauxetic effect, also known as differential radial expansion,[3] in this complex arising from large covalency differences between the octahedral t_{2g} and e_g orbitals, the latter orbitals experiencing greater metal−ligand covalency due to their σ antibonding character. As a consequence, lower values of the Racah *B* and *C* interelectron repulsion parameters were required to fit the spin-forbidden $^3A_{2g} \rightarrow {}^1E_g$ and $^3A_{2g} \rightarrow {}^1A_{1g}$ transitions which involve spin-flips within the e_g orbitals.

In order to examine the consequences of spin−orbit mixing and differential nephelauxetic effects in octahedral Ni(II) complexes more fully, we now report the electronic spectra and ligand-field analysis of the Ni(II) complexes involving the

† The Australian National University.
‡ Centre for Magnetic Resonance, The University of Queensland.
§ Department of Chemistry, The University of Queensland.
|| The University of Sydney.
⊗ Abstract published in *Advance ACS Abstracts,* July 1, 1997.

(1) (a) Stranger, R.; Wallis, S. C.; Gahan, L. R.; Kennard, C. H. L.; Byriel, K. A. *J. Chem. Soc., Dalton Trans.* **1992**, 2971. (b) Donlevy, T. M.; Gahan, L. R.; Stranger, R.; Kennedy, S. E.; Byriel, K. A.; Kennard, C. H. L. *Inorg. Chem.* **1993**, *32*, 6023.

(2) (a) Jørgensen, C. K. *Acta Chem. Scand.* **1955**, *9*, 1362. (b) Palmer, R. A.; Piper, T. S. *Inorg. Chem.* **1966**, *5*, 864. (c) Dingle, R.; Palmer, R. A. *Theor. Chim. Acta* **1966**, *6*, 249. (d) Alper, J. S.; Zompa, L. J. *Inorg. Nucl. Chem.* **1980**, *42*, 1693. (e) Hart, S. M.; Boeyans, J. C. A.; Hancock, R. D. *Inorg. Chem.* **1983**, *22*, 982. (f) Gahan, L. R.; Hambley, T. W. *Transition Met. Chem. (N.Y.)* **1988**, *13*, 72. (g) Liehr, A. D.; Ballhausen, C. J. *Ann. Phys.* **1959**, *6*, 134. (h) Zompa, L. J. *Inorg. Chem.* **1978**, *17*, 2531. (i) Yang, R.; Zompa, L. J. *Inorg. Chem.* **1976**, *15*, 1499. (j) Martin, L. L.; Martin, R. L.; Murray, K. S.; Sargeson, A. M. *Inorg. Chem.* **1990**, *29*, 1387.

(3) Jørgensen, C. K. *Absorption Spectra and Chemical Bonding in Complexes*; Pergamon Press: Oxford, U.K., 1962.

S0020-1669(96)01453-X CCC: $14.00 © 1997 American Chemical Society

Chart 1

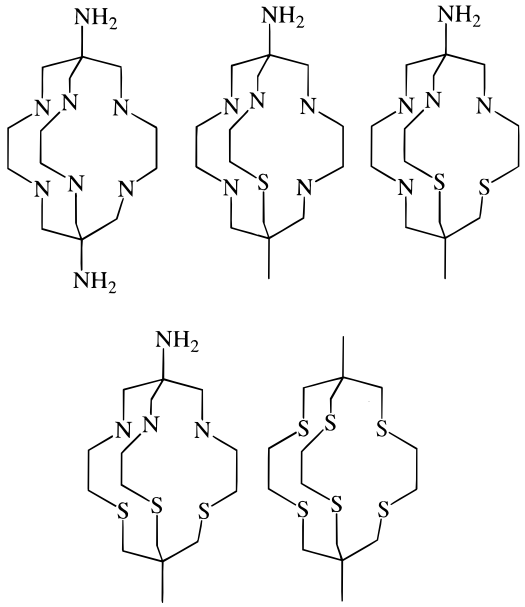

encapsulating ligands diAMN_6sar, AMN_5Ssar, AMN_4S_2sar, AMN_3S_3sar, and Me_2S_6sar shown in Chart 1. As the [Ni(AMN_5Ssar)]$^{2+}$ complex is new, we also report the crystal structure of its perchlorate salt [Ni(AMN_5Ssar)]$(ClO_4)_2$. These complexes provide a particularly useful series in relation to the present investigation as the number of nitrogen and sulfur donors can be systematically varied through Ni($N_{6-x}S_x$) ($x = 0-6$) coordination with the macrocyclic backbone structure remaining essentially unchanged. As the number of sulfur donors increases through the series, one anticipates a corresponding increase in the metal−ligand covalency. This should manifest itself in a greater differential nephelauxetic effect as well as large changes in the energy of the spin-forbidden $^3A_{2g} \rightarrow {}^1E_g$ transition and, as a result, the extent of spin−orbit mixing between the ^1E_g and $^3T_{2g}$ states.

Experimental Section

Detailed synthesis and characterization of the metal-free ligand AMN_5Ssar have been reported.[4] The abbreviations employed in this work to describe the ligand and the complex have been described previously.[5]

Caution! Perchlorate salts of metal complexes can be explosive and should be handled with care. They should not be heated as solids.

[Ni(AMN_5Ssar)]$(ClO_4)_2$. The ligand AMN_5Ssar (0.48 g) was dissolved in methanol (10 mL), and nickel perchlorate (0.58 g) was added slowly with stirring. The solution was warmed and stirring continued for 0.25 h, during which a purple precipitate formed. Dropwise addition of water resulted in a purple solution with a small amount of a green precipitate, which was removed by filtration. $LiClO_4$ was added to the filtrate, and upon standing, purple crystals were deposited. The product was isolated by filtration and dried in air (0.33 g). Anal. Calcd for [Ni($C_{15}H_{34}N_6S$)]$(ClO_4)_2$: C, 30.6; H, 5.83; N, 14.3. Found: C, 28.5; H, 6.06; N, 13.2.

X-ray Crystallography. Crystals for diffractometry were mounted on glass fibers with cyanoacrylate resin. Lattice parameters at 21 °C were determined by least-squares fits to the setting parameters of 25 independent reflections, measured and refined on an Enraf-Nonius CADF-4 four-circle diffractometer with a graphite monochromator. Intensity data were collected in the range $1 < \theta < 25°$. Data were reduced, and Lorentz, polarization, and numerical absorption corrections were applied using the Enraf-Nonius structure determination package.[6] The structures were solved using direct methods in SHELXS-86[7] and refined by full-matrix least-squares procedures with SHELX-76.[8] Neutral-atom scattering factors were used.[9] Hydrogen atoms were included at calculated sites with fixed isotropic thermal parameters, and all other atoms were refined anisotropically. Plots were drawn with ORTEP.[10] The crystal data are reported in Table 1.

Table 1. Crystal Data for [Ni(AMN_5Ssar)]$(CLO_4)_2$

space group	$P2_1/a$
crystal system	monoclinic
a (Å)	17.160(3)
b (Å)	8.740(3)
c (Å)	18.198(3)
β (deg)	108.73(2)
Z	4
V (Å^3)	2729
fw	588.17
empirical formula	$C_{15}H_{34}N_6NiSCl_2O_8$
temp (°C)	25
crystal color	pink
crystal habit	needles
ρ_{calc} (g/cm^3)	1.511
radiation (λ (Å))	Mo Kα (0.710 69 Å)
monochromator	graphite
2θ range (deg)	1−120
no. of reflns measd	4300
no. of reflns used	2904
no. of variables	360
R	0.043
R_w	0.034

Electronic Spectroscopy. The absorption spectra of the Ni(II) complexes dissolved in DMF were measured in Nafion film, a perfluorinated membrane, at room temperature and ~10 K using a Cary 17 spectrophotometer modified to allow data acquisition and control by a computer. The Nafion film samples were cooled to ~10 K using a Leybold-Heraeus ROK 10-300 closed-cycle helium cryostat system. Baseline spectra were recorded under identical conditions using a blank Nafion film sample. Data analysis and spectral deconvolution were carried out using the software packages SpectraCalc by Galactic Industries and PeakFit by Jandel Scientific. Standard ligand-field calculations (without differential covalency corrections) were undertaken using the Fortran program CAMMAG.[11]

Results and Discussion

X-ray Crystallography. The structure of the compound consists of the complex cation and two perchlorate anions. The molecular structure of the cation [Ni(AMN_5Ssar)]$^{2+}$ with its numbering scheme is shown in Figure 1. Final positional parameters and selected bond distances and angles are reported in Tables 2−4, respectively. The Ni−N distances for [Ni(AMN_5Ssar)]$^{2+}$ (average 2.110 Å) are very similar to those reported for the hexaamine encapsulating complexes[12]

(4) Bruce, J. I.; Gahan, L. R.; Hambley, T. W.; Stranger, R. *Inorg. Chem.* **1993**, *32*, 5997.
(5) Donlevy, T. M.; Gahan, L. R.; Hambley, T. W.; Stranger, R. *Inorg. Chem.* **1992**, *31*, 4376.
(6) *Enraf-Nonius Structure Determination Package*; Enraf-Nonius: Delft, Holland, 1985.
(7) Sheldrick, G. M. SHELXS-86, Program for Solution of Crystal Structures. University of Gottingen, 1986.
(8) Sheldrick, G. M. SHELX-76, Program for Crystal Structure Determination. University of Cambridge, 1976.
(9) Ibers, J. A., Hamilton, W. C., Eds. *International Tables for X-ray Crystallography*; Kynoch Press: Birmingham, U.K., 1974; Vol. IV.
(10) Johnson, C. K. *ORTEP: A Thermal Ellipsoid Plotting Program*; Oak Ridge National Laboratory: Oak Ridge, TN, 1965.
(11) Cruse, D. A.; Davies, J. E.; Gerloch, M.; Harding, J. H.; Mackey, D. J.; McMeeking, R. F. CAMMAG, a Fortran Computing Package. University Chemical Laboratory, Cambridge, 1979.
(12) (a) Comba, P.; Sargeson, A. M.; Engelhardt, L. M.; Harrowfield, J. M.; White, A. H.; Horn, E.; Snow, M. R. *Inorg. Chem.* **1985**, *24*, 2325. (b) Comba, P. *Inorg. Chem.* **1989**, *28*, 426. (c) Clark, I. J.; Creaser, I. I.; Engelhardt, L. M.; Harrowfield, J. M.; Krausz, E. R.; Moran, G. M.; Sargeson, A. M.; White, A. M. *Aust. J. Chem.* **1993**, *46*, 111. (d) Engelhardt, L. M.; Harrowfield, J. M.; Sargeson, A. M.; White, A. H. *Aust. J. Chem.* **1993**, *46*, 127. (e) Suh, M. P.; Shin, W.; Kim, D.; Kim, S. *Inorg. Chem.* **1984**, *23*, 618.

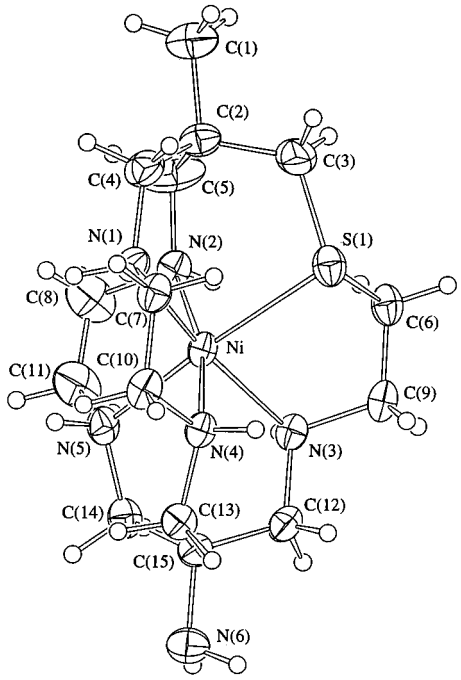

Figure 1. Numbering scheme for the complex cation $[Ni(AMN_5Ssar)]^{2+}$.

Table 2. Non-Hydrogen Positional Parameters for $[Ni(AMN_5Ssar)](ClO_4)_2$

atom	*x*	*y*	*z*	*B*(eq) (Å^2)
Ni	0.77112(4)	0.01720(8)	0.23341(4)	3.23(3)
Cl(1)	0.62909(8)	0.0274(1)	0.86991(8)	4.59(5)
Cl(2)	0.45090(9)	−0.1371(2)	0.61970(8)	5.48(6)
S(1)	0.66304(8)	−0.1175(1)	0.13532(7)	4.42(5)
O(1)	0.5760(6)	−0.081(1)	0.8175(7)	9.6(6)
O(2)	0.6889(7)	0.071(2)	0.8418(8)	8.7(8)
O(3)	0.659(2)	−0.052(3)	0.940(1)	7.4(8)
O(4)	0.564(1)	0.149(2)	0.874(1)	5.2(5)
O(5)	0.632(1)	−0.037(2)	0.7997(6)	9.3(8)
O(6)	0.7038(8)	0.120(2)	0.8949(7)	7.9(6)
O(7)	0.636(2)	−0.081(3)	0.926(1)	8(1)
O(8)	0.581(1)	0.130(3)	0.862(2)	8.5(8)
O(9)	0.4683(2)	−0.2598(4)	0.6738(2)	7.6(2)
O(10)	0.3923(3)	−0.1834(7)	0.5497(3)	11.8(3)
O(11)	0.5235(3)	−0.0925(5)	0.6058(3)	10.1(3)
O(12)	0.4194(2)	−0.0103(4)	0.6505(2)	7.2(2)
O(13)	0.3425(2)	0.3962(5)	0.5645(2)	7.5(2)
O(14)	0.2655(2)	0.1084(5)	0.5321(2)	7.3(2)
N(1)	0.7769(2)	0.1651(4)	0.1434(2)	3.7(2)
N(2)	0.6857(2)	0.1684(4)	0.2575(2)	3.8(2)
N(3)	0.8551(2)	0.1215(4)	0.3309(2)	4.0(2)
N(4)	0.8719(2)	−0.0887(4)	0.2134(2)	3.4(1)
N(5)	0.7616(2)	−0.1665(4)	0.3060(2)	3.6(2)
N(6)	0.9895(3)	−0.2127(6)	0.4152(3)	5.2(2)
C(1)	0.5532(3)	0.2989(7)	0.0551(3)	6.5(3)
C(2)	0.6209(3)	0.2002(6)	0.1109(3)	4.4(2)
C(3)	0.5924(3)	0.0339(7)	0.0913(3)	5.9(3)
C(4)	0.6985(3)	0.2333(6)	0.0913(3)	5.1(2)
C(5)	0.6249(4)	0.2461(7)	0.1921(3)	8.1(4)
C(6)	0.6252(3)	−0.2033(5)	0.2082(3)	4.3(2)
C(7)	0.8213(3)	0.0756(5)	0.1003(3)	4.2(2)
C(8)	0.7363(4)	0.2811(7)	0.3107(4)	7.4(3)
C(9)	0.6971(3)	−0.2799(5)	0.2658(3)	4.4(2)
C(10)	0.8964(3)	0.0075(5)	0.1580(3)	4.1(2)
C(11)	0.8065(4)	0.2263(7)	0.3643(3)	7.2(3)
C(12)	0.9057(3)	0.0147(6)	0.3896(3)	4.3(2)
C(13)	0.9414(3)	−0.1274(5)	0.2836(3)	4.0(2)
C(14)	0.8414(3)	−0.2449(5)	0.3445(3)	4.2(2)
C(15)	0.9171(3)	−0.1417(5)	0.3572(3)	3.8(2)

$[Ni(diAMN_6sarH_2)](NO_3)_4\cdot H_2O$ (Ni−N_{av} = 2.109(5) Å), $[Ni(diAMN_6sarH_2)]Cl_4\cdot H_2O$ (Ni−N_{av} = 2.111(5) Å), and $[Ni(diAZAN_6sar)]^{2+}$ (Ni−N_{av} = 2.105(5) Å) and the mixed nitrogen−sulfur complex $[Ni(AMN_4S_2sar)]^{2+}$ (Ni−N_{av} = 2.103(12) Å).[1b] The Ni−S bond length of 2.426 Å is comparable to those reported for $[Ni(AMN_4S_2sar)]^{2+}$ (Ni−S_{av} = 2.398(5) Å).

Table 3. Selected Bond Distances (Å) for $[Ni(AMN_5Ssar)](ClO_4)_2$

Ni−S(1)	2.426(1)	Ni−N(1)	2.114(3)
Ni−N(2)	2.121(3)	Ni−N(5)	2.101(4)
N(1)−C(4)	1.499(6)	Ni−N(4)	2.094(3)
N(1)−C(7)	1.481(5)	Ni−N(3)	2.118(3)
N(2)−C(5)	1.472(6)	N(2)−C(8)	1.457(6)
N(5)−C(11)	1.492(6)	N(5)−C(14)	1.474(6)
N(4)−C(10)	1.474(5)	N(4)−C(13)	1.479(5)
N(3)−C(9)	1.492(5)	N(3)−C(12)	1.489(5)
N(6)−C(15)	1.485(6)	S(1)−C(3)	1.800(5)
S(1)−C(6)	1.816(5)	C(1)−C(2)	1.539(6)
C(2)−C(3)	1.538(7)	C(2)−C(4)	1.514(6)
C(13)−C(15)	1.531(6)	C(2)−C(5)	1.511(7)
C(12)−C(15)	1.536(6)	C(6)−C(9)	1.496(6)
C(7)−C(10)	1.499(6)	C(8)−C(11)	1.370(7)

Table 4. Selected Bond Angles (deg) for $[Ni(AMN_5Ssar)](ClO_4)_2$

S(1)−Ni−N(1)	86.7(1)	S(1)−Ni−N(2)	92.2(1)
S(1)−Ni−N(5)	170.7(1)	S(1)−Ni−N(4)	97.9(1)
S(1)−Ni−N(3)	84.1(1)	N(1)−Ni−N(2)	89.2(1)
N(1)−Ni−N(5)	101.5(1)	N(1)−Ni−N(4)	83.6(1)
N(1)−Ni−N(3)	168.2(1)	N(2)−Ni−N(5)	83.5(1)
N(2)−Ni−N(4)	167.3(1)	N(2)−Ni−N(3)	98.4(1)
N(5)−Ni−N(4)	87.6(1)	N(3)−Ni−N(5)	88.4(1)
N(4)−Ni−N(3)	90.4(1)	Ni−S(1)−C(3)	102.6(2)
Ni−S(1)−C(6)	91.8(2)	C(3)−S(1)−C(6)	106.3(2)
Ni−N(5)−C(11)	106.8(3)	Ni−N(3)−C(14)	114.9(3)
C(11)−N(5)−C(14)	111.7(4)	Ni−N(4)−C(10)	107.4(3)
Ni−N(4)−C(13)	115.7(3)	C(10)−N(4)−C(13)	113.2(3)
Ni−N(3)−C(9)	113.0(3)	Ni−N(3)−C(12)	113.5(3)
Ni−N(1)−C(4)	118.5(3)	Ni−N(1)−C(7)	104.3(3)
C(9)−N(3)−C(12)	110.5(4)	C(4)−N(1)−C(7)	112.6(4)
Ni−N(2)−C(5)	118.6(3)	Ni−N(2)−C(8)	104.8(3)
C(5)−N(2)−C(8)	110.0(4)	C(1)−C(2)−C(3)	105.1(4)
C(1)−C(2)−C(4)	105.7(4)	C(1)−C(2)−C(5)	106.5(4)
C(3)−C(2)−C(4)	111.3(4)	C(3)−C(2)−C(5)	113.0(5)
N(1)−C(7)−C(10)	108.2(4)	C(4)−C(2)−C(5)	114.4(5)
S(1)−C(3)−C(2)	118.2(3)	N(2)−C(8)−C(11)	115.9(5)
N(1)−C(4)−C(2)	117.0(4)	N(3)−C(9)−C(6)	111.2(4)
N(2)−C(5)−C(2)	117.7(4)	N(4)−C(10)−C(7)	109.6(4)
S(1)−C(6)−C(9)	106.7(3)	N(6)−C(15)−C(14)	106.3(4)
N(6)−C(15)−C(13)	104.7(4)	N(5)−C(11)−C(8)	113.8(5)
N(6)−C(15)−C(12)	109.6(4)	C(14)−C(15)−C(13)	111.7(4)
C(12)−C(15)−C(14)	112.2(4)	C(13)−C(15)−C(12)	111.8(4)
N(5)−C(14)−C(15)	114.0(4)	N(4)−C(13)−C(15)	113.8(4)
N(3)−C(12)−C(15)	113.9(4)		

The N(5) nitrogen atom *trans* to the lone sulfur exhibits a considerable deviation from an "axial" position. The N(5)−Ni−N(1) bond angle, where N(1) is *cis* to N(5), is 101.5°. Similarly, the N(2)−Ni−N(5) bond angle, where N(2) is *cis* to N(5), shows a significant reduction (83.5°), but the angles N(3)−Ni−N(5) and N(5)−Ni−N(4) are not reduced to the same extent (88.4, and 87.6°, respectively). The atoms in the coordination sphere of the nickel ion do not lie directly *trans* to each other, and all of the angles are much less than 180°, with the N(2)−Ni−N(4), N(1)−Ni−N(3), and S(1)−Ni−N(5) angles reduced to 167.3, 168.2, and 170.7°, respectively.

The hybridization of the capping carbons is expected to be tetrahedral. The unsymmetrical nature of the ligand increases the normal sp^3 bond angles of 109.5°; the angles about the C(2) carbon are 111.3, 113.0, and 114.4° for C(3)−C(2)−C(4), C(3)−C(2)−C(5), and C(4)−C(2)−C(5), respectively. The same feature is observed for the quaternary carbon connected to the amine cap, where angles to the carbons labeled C(14), C(13), and C(12) are 111.7, 112.2, and 111.8°, respectively.

Electronic Spectroscopy. The low-temperature (∼10 K) absorption spectra of the encapsulating complexes $[Ni(diAMN_6sar)]^{2+}$, $[Ni(AMN_5Ssar)]^{2+}$, $[Ni(AMN_4S_2sar)]^{2+}$, and [Ni-

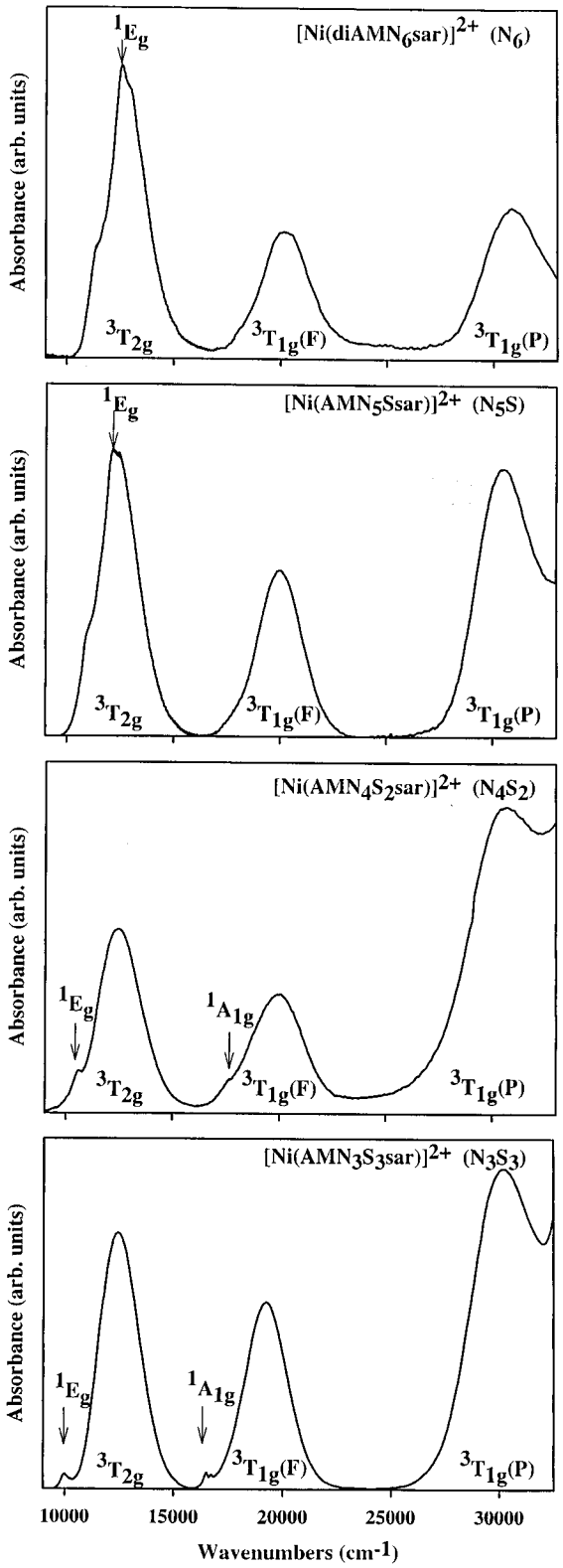

Figure 2. Low-temperature (~10 K) absorption spectra (in Nafion film) of the Ni(II)-encapsulating complexes involving $N_{6-x}S_x$ ($x = 0-3$) coordination.

$(AMN_3S_3sar)]^{2+}$ in Nafion film are shown in Figure 2. The low-temperature spectra exhibit improved resolution. For example, in the case of $[Ni(AMN_3S_3sar)]^{2+}$, the room-temperature spectrum does not clearly reveal the weak $^3A_{2g} \rightarrow {}^1E_g$ and $^3A_{2g} \rightarrow {}^1A_{1g}$ spin-forbidden transitions but at low temperatures both transitions are well resolved, including fine structure associated with the latter. Furthermore, in the room-temperature spectra of the complexes involving thioether coordination, the highest energy spin-allowed transition, $^3A_{2g} \rightarrow {}^3T_{1g}(P)$, is often partly obscured by intense low-lying charge transfer bands around 37 000 cm^{-1}. At low temperatures, however, the $^3A_{2g} \rightarrow {}^3T_{1g}(P)$ transition is reasonably well resolved in all cases except for the $[Ni(Me_2S_6sar)]^{2+}$ complex, where the lowest energy charge transfer band is observed at ~30 000 cm^{-1}. The resolution of all three spin-allowed transitions and at least one of the spin-forbidden transitions is necessary to obtain reliable ligand-field parameters as well as an indication of the extent of the differential nephelauxetic effect. The positions and ligand-field assignments for the observed d−d and charge transfer bands are given in Table 5.

From the reported absorption spectra of Ni(II) macrocyclic complexes involving nitrogen and sulfur coordination,[13] it is apparent that the amine and thioether donor ligands exert comparable ligand field strengths. However, in the absence of geometric constraints imposed by the macrocyclic backbone, one would expect the thioether ligand to be a much weaker donor, consistent with the lower 10*Dq* values found for the larger and more flexible ring systems.[14] Apart from these systems, the 10*Dq* values found for mixed nitrogen and sulfur donor complexes of Ni(II) generally fall within the range 11 500−12 500 cm^{-1}. Consequently, the position of the lowest energy spin-allowed band, $^3A_{2g} \rightarrow {}^3T_{2g}$, which is only dependent on 10*Dq*, should not change dramatically as the number of nitrogen and sulfur donors is allowed to vary. Examination of the spectra of the Ni(II)-encapsulated complexes shown in Figure 2 establishes that this is indeed the case. The position of the lowest energy spin-allowed band remains relatively unchanged at approximately 12 500 cm^{-1} except for the case of the $[Ni(Me_2S_6sar)]^{2+}$ complex, where the same transition occurs nearly 1000 cm^{-1} higher in energy. The larger 10*Dq* value for this complex presumably arises from shorter Ni−S bond distances.

In contrast to the spin-allowed $^3A_{2g} \rightarrow {}^3T_{2g}$ transition, the energies of the spin-forbidden $^3A_{2g} \rightarrow {}^1E_g$ and $^3A_{2g} \rightarrow {}^1A_{1g}$ transitions depend largely on the Racah *B* and *C* interelectron repulsion parameters and to a much smaller extent on 10*Dq*. As the number of sulfur donors increases, both spin-forbidden transitions should be progressively lowered in energy due to the reduction in the Racah *B* and *C* parameters arising from the increased metal−ligand covalency associated with the thioether ligand. This prediction is borne out in Figure 3, which shows the room-temperature absorption spectra of the complexes $[Ni(NH_3)_6]^{2+}$ and $[Ni([9]aneS_3)_2]^{2+}$, comprising N_6 and S_6 coordination, respectively, of Ni(II). From the spectra, the position of the spin-forbidden $^3A_{2g} \rightarrow {}^1E_g$ transition moves from approximately 13 300 cm^{-1} in $[Ni(NH_3)_6]^{2+}$ to 8500 cm^{-1} in $[Ni([9]aneS_3)_2]^{2+}$, corresponding to a reduction of nearly 5000 cm^{-1} associated with the change from N_6 to S_6 coordination. The same trend is also observed in the spectra of the encapsulating complexes shown in Figure 2.

The behavior of the higher energy $^3A_{2g} \rightarrow {}^1A_{1g}$ spin-forbidden transition is not as obvious because of significant overlap with the spin-allowed $^3A_{2g} \rightarrow {}^3T_{1g}(F)$ transition. However, in the low-temperature absorption spectrum[2c] of $[Ni(en)_3]^{2+}$, the $^3A_{2g} \rightarrow {}^1A_{1g}$ spin-forbidden transition is observed around 22 500 cm^{-1} whereas, in the spectrum of $[Ni(AMN_3S_3sar)]^{2+}$ shown in Figure 2, it clearly occurs to much lower energy at approximately 16 500 cm^{-1}. Thus, in going from N_6 to N_3S_3 coordination of Ni(II), a reduction of approximately 6000 cm^{-1}

(13) (a) McAuley, A.; Subramanian, S. *Inorg. Chem.* **1990**, *29*, 2831. (b) Chandrasekhar, S.; McAuley, A. *J. Chem. Soc., Dalton Trans.* **1992**, 2967. (c) Urbanyak, P.; Gzheidzyak, A.; Dzegets, Yu. *Russ. J. Coord. Chem. (Engl. Transl.)* **1994**, *20*, 483.
(14) Grant, G. J.; Grant, C. D.; Setzer, W. N. *Inorg. Chem.* **1991**, *30*, 353.

Table 5. Band Assignments and Ligand-Field Parameters for Nickel(II)-Encapsulating Complexes

nickel(II) complex		d−d transition energy (cm^{-1})					charge transfer energy (cm^{-1})			ligand-field parameters			
ligand	coordn	$^3A_{2g} \rightarrow {}^3T_{2g}$	$^3A_{2g} \rightarrow {}^3T_{1g}(F)$	$^3A_{2g} \rightarrow {}^3T_{1g}(P)$	$^3A_{2g} \rightarrow {}^1E_g$	$^3A_{2g} \rightarrow {}^1A_{1g}$	S → Ni	(S,N) → Ni	N → Ni	*B*	*C*	*C*/*B*	10*Dq*
diAMN$_6$sar	N_6	12 725	20 360	31 100	12 505	not obs				826	3101	3.8	12940
AMN$_5$Ssar	N_5S	12 440	19 995	30 525	10 890	not obs		39 650	44 600	816	2933	3.6	12680
AMN$_4$S$_2$sar	N_4S_2	12 730	19 900	30 660	10 485	17 515		36 580 38 420	45 175	795	2206	2.8	12830
AMN$_3$S$_3$sar	N_3S_3	12 425	19 180	30 135	9 980	16 515		35 555 37 380		762	2074	2.7	12640
Me$_2$S$_6$sar	S_6	13 675	19 885	not obs	8 365	not obs	30 695			653	1660	2.5	13670

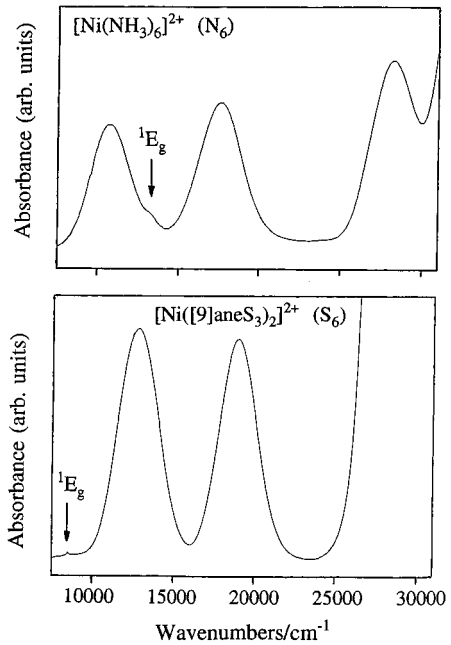

Figure 3. Solution spectra of $[Ni(NH_3)_6]^{2+}$ and $[Ni([9]aneS_3)_2]^{2+}$.

has occurred compared to 3300 cm^{-1} for the $^3A_{2g} \rightarrow {}^1E_g$ spin-forbidden transition. However, the relative reduction of both transitions is similar, as is predicted from their dependence on the Racah interelectron repulsion parameters.[1b]

Charge Transfer Spectra. A simplistic view, taking account of the mixed-donor complexes, predicts three different types of σ(L) → Ni LMCT transitions, namely σ(S) → Ni, σ(S,N) → Ni, and σ(N) → Ni in order of increasing energy. The σ(S,N) → Ni charge transfer transition is associated with nitrogen and sulfur donors which are trans to one another. In the mixed-donor complexes $[Ni(AMN_5Ssar)]^{2+}$, $[Ni(AMN_4S_2sar)]^{2+}$, and $[Ni(AMN_3S_3sar)]^{2+}$, the σ(S) → Ni charge transfer should not occur, as all sulfur donors are trans to nitrogen donors. In addition, the σ(N) → Ni charge transfer transition should not occur in $[Ni(AMN_3S_3sar)]^{2+}$, as all nitrogen donors are trans to sulfur donors. On the whole, on the basis of the charge-transfer spectra shown in Figure 4 and assignments given in Table 5, these rather crude predictions seem to be borne out. The σ(S) → Ni and σ(N) → Ni charge transfer transitions are generally observed at approximately 30 000 and 45 000 cm^{-1}, respectively, while the mixed-donor σ(S,N) → Ni charge transfer transitions are observed between 36 000 and 39 000 cm^{-1}. As seen in Figure 4, the band center associated with the σ(S,N) → Ni charge transfer transitions also undergoes a red shift as the number of S donors increases. The additional structure observed on some of these bands can quite reasonably be attributed to distortions away from octahedral symmetry and multiplet splittings arising from interelectron repulsion effects.

Spin−Orbit Mixing. From a detailed analysis of the $^3A_{2g} \rightarrow {}^3T_{2g}$ transition in $[Ni([9]aneN_3)_2]^{2+}$, we were able to establish that appreciable spin−orbit mixing occurred between the ^1E_g and $^3T_{2g}$ states in this complex.[1a] As a consequence, the $^3A_{2g} \rightarrow {}^1E_g$ spin-forbidden transition gains significant intensity from the spin-allowed $^3A_{2g} \rightarrow {}^3T_{2g}$ transition, leading to the appearance of a double-humped band envelope. In order to explain this mechanism more fully, it is necessary to examine the effects of spin−orbit coupling on the $^3T_{2g}$ and ^1E_g states.

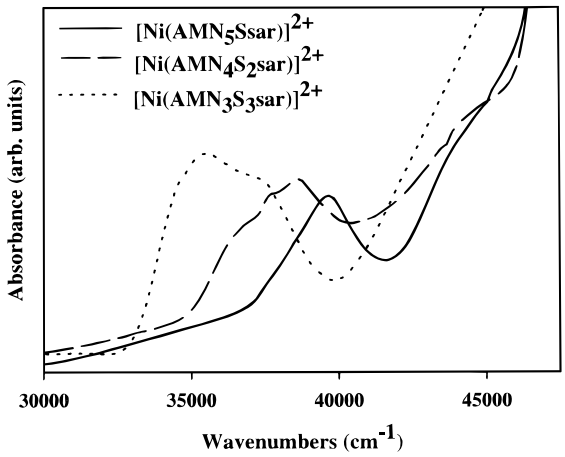

Figure 4. Absorption spectra showing charge transfer bands for $[Ni(AMN_5Ssar)]^{2+}$, $[Ni(AMN_4S_2sar)]^{2+}$, and $[Ni(AMN_3S_3sar)]^{2+}$.

In octahedral (O_h) symmetry, the $^3T_{2g}$ state comprises $A_2 + E + T_1 + T_2$ spin−orbit levels whereas the ^1E_g state consists of just one E spin−orbit level. Since the spin−orbit coupling operator is symmetry invariant, it can only mix spin−orbit levels of the same symmetry. Therefore, only the E spin−orbit level of the $^3T_{2g}$ state can mix with the ^1E_g state in the octahedral limit. The closer these two spin−orbit levels approach one another, the greater the mixing between them and consequent enhancement in the intensity of the $^3A_{2g} \rightarrow {}^1E_g$ spin-forbidden transition. As a result of spin−orbit mixing, the normally weak and sharp band associated with the spin-forbidden transition to the ^1E_g state (*cf.* spectrum of $[Ni([9]aneS_3)_2]^{2+}$ in Figure 3) broadens and intensifies whereas the broad band associated with the spin-allowed transition to the E spin−orbit level of the $^3T_{2g}$ state loses intensity and narrows. In the realm of appreciable spin−orbit mixing, this interaction will give rise to two weaker and narrower bands superimposed on a broad but more intense band resulting from transitions to the remaining spin−orbit components of the $^3T_{2g}$ state.

The above situation occurs in the electronic spectrum of $[Ni([9]aneN_3)_2]^{2+}$, accounting for the double-humped band shape associated with the spin-allowed $^3A_{2g} \rightarrow {}^3T_{2g}$ transition. In this complex, spin−orbit mixing is effectively maximized, leading to approximately equal intensities for the transitions to the spin-forbidden ^1E_g state and the E spin−orbit level of the $^3T_{2g}$ state. It should be noted, however, that since the ^1E_g state is mixed with only the E spin−orbit level of the $^3T_{2g}$ state, it is not possible for the $^3A_{2g} \rightarrow {}^1E_g$ spin-forbidden transition to gain intensity comparable to the $^3A_{2g} \rightarrow {}^3T_{2g}$ spin-allowed transition. At best, assuming all the spin−orbit components of the $^3T_{2g}$ state contribute equal intensity, the maximum intensity that the $^3A_{2g} \rightarrow {}^1E_g$ transition can borrow is only about 10%. Thus,

the nature of the double-humped band shape observed in $[Ni([9]aneN_3)_2]^{2+}$ and other Ni(II) complexes such as $[Ni(bipy)_3]^{2+}$ and $[Ni(phen)_3]^{2+}$ is not so much the result of an appreciable gain in intensity of the $^3A_{2g} \rightarrow {}^1E_g$ spin-forbidden transition as it is of the narrow bandwidths associated with transitions to the ^1E_g state and E spin−orbit level of the $^3T_{2g}$ state, both of which contain significant spin-singlet character due to spin−orbit mixing.

An examination of the lowest energy transition in the absorption spectra of the Ni(II)-encapsulating complexes shown in Figure 2 suggests that spin−orbit mixing effects are also operative in these systems, particularly for $[Ni(diAMN_6sar)]^{2+}$ and $[Ni(AMN_5Ssar)]^{2+}$. To test this conclusion, the $^3A_{2g} \rightarrow {}^3T_{2g}$ band envelope in all four encapsulating complexes was deconvoluted in order to locate the component bands. The results of this analysis are shown in Figure 5. In each case, the band envelope was fitted to three Gaussian components, one of which was skewed to account for the higher energy shoulder of the band envelope. The two smaller symmetric Gaussian components correspond to transitions to the spin-forbidden ^1E_g state and the E spin−orbit level of the $^3T_{2g}$ state, while the larger skewed Gaussian component is associated with transitions to the remaining $A_2 + T_1 + T_2$ spin−orbit levels of the $^3T_{2g}$ state. In the case of $[Ni(AMN_4S_2sar)]^{2+}$ and $[Ni(AMN_3S_3sar)]^{2+}$, it is possible to obtain a reasonable fit to the band envelope using only two Gaussian components, the larger of which is skewed. However, for continuity, the band envelopes were deconvoluted using three components, consistent with the spin−orbit mixing model discussed above. Clearly, for these two complexes the uncertainity in both the position and the intensity of the guassian component associated with the E spin−orbit level of the $^3T_{2g}$ state is more significant.

The results of the band analysis shown in Figure 5 nicely illustrate the gradual intensity transfer from the E spin−orbit component of the $^3T_{2g}$ state to the ^1E_g state as these two levels first approach one another and then move away in response to the progressive increase in sulfur donors. Initially, in $[Ni(diAMN_6sar)]^{2+}$, the ^1E_g state lies to higher energy (∼12 500 cm^{-1}) and is significantly weaker than the E spin−orbit component of the $^3T_{2g}$ state, denoted $^3T_{2g}(E)$ in Figure 5. In $[Ni(AMN_5Ssar)]^{2+}$, the replacement of a nitrogen donor with sulfur results in a lowering of ^1E_g state energy to ∼12 000 cm^{-1} and, consequently, greater interaction with the $^3T_{2g}(E)$ spin−orbit level, as evidenced by the intensity gain of the ^1E_g state relative to $^3T_{2g}(E)$. In fact, for this complex, the spin−orbit mixing is almost maximized because the two Gaussian components have nearly equal intensities. In $[Ni(AMN_4S_2sar)]^{2+}$, the two levels have effectively crossed with the higher energy Gaussian component, assigned to $^3T_{2g}(E)$, now carrying the greater intensity. Finally, in $[Ni(AMN_3S_3sar)]^{2+}$, the ^1E_g state (observed at ∼10 000 cm^{-1}) has moved well away from $^3T_{2g}$-(E) level and is now much weaker and sharper relative to the $^3T_{2g}(E)$ level, indicative of a significant reduction in spin−orbit mixing between these two states.

The above analysis is, to some extent, dependent on the complexes maintaining approximate octahedral symmetry. Since the nitrogen and thioether donors have similar ligand-field strengths, any significant departure from octahedral symmetry must arise through geometric distortions of the L−Ni−L′ bond angles away from 90°. Examination of the relevant bond angles for $[Ni(AMN_5Ssar)]^{2+}$ given in Table 4 reveals that the deviation of the L−Ni−L′ bond angles from 90° can be as much as 11°. However, since the low-temperature Nafion film spectra of the encapsulating complexes do not exhibit any pronounced low-symmetry splitting of the spectral bands, in particular for the $^3T_{2g}-{}^1E_g$ band envelope, the assumption of approximate octahedral symmetry in these complexes is reasonable. This is in accord with previous ligand-field calculations[1b] using the angular-overlap model on the $[Ni(AMN_4S_2sar)]^{2+}$ complex, which showed that the low-symmetry splitting of the $^3T_{2g}$ state was less than 300 cm^{-1}.

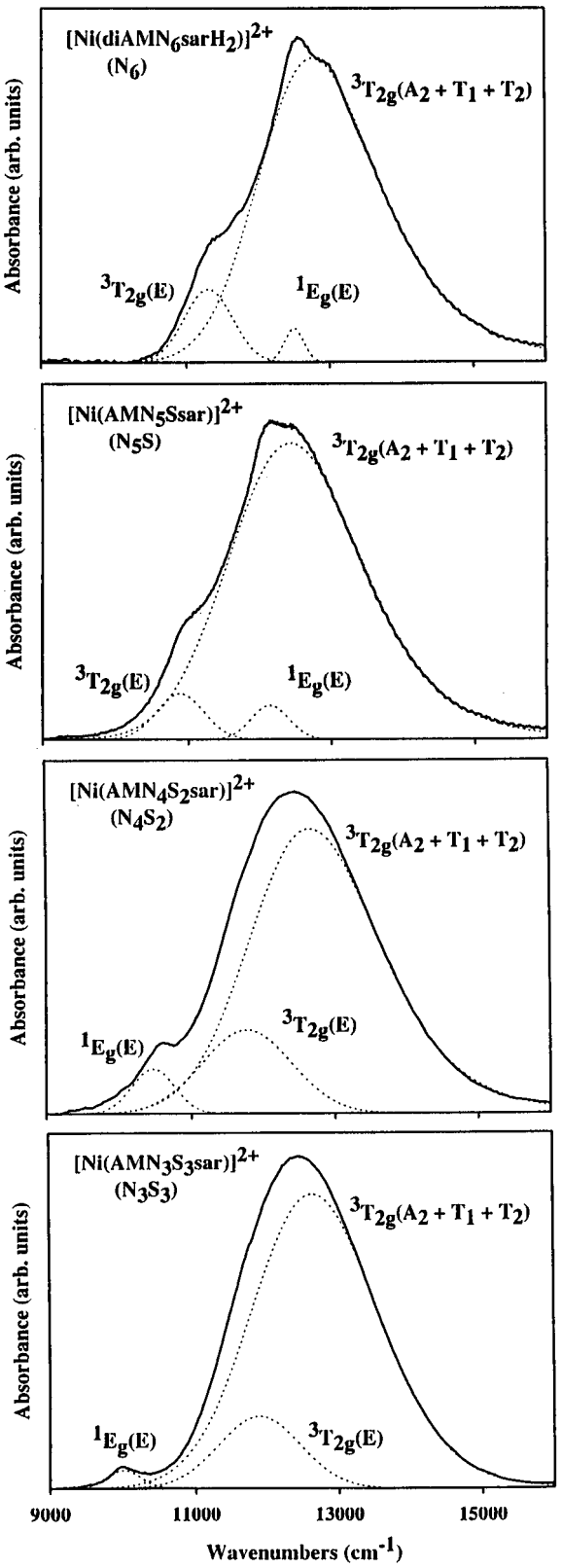

Figure 5. Analysis of the low-temperature (∼10 K) band shape for the $^3A_{2g} \rightarrow {}^3T_{2g}$ transition in the Ni(II)-encapsulating complexes involving $N_{6-x}S_x$ ($x = 0-3$) coordination.

It is worth noting that a similar spin−orbit mixing phenomenon is possible between the spin-forbidden $^3A_{2g} \rightarrow {}^1A_{1g}$ and

Table 6. Comparison of Normal and Differential Covalency Ligand-Field Models

assignment		$[Ni(NH_3)_6]^{2+}$			$[Ni(AMN_3S_3sar)]^{2+}$		
O_h state	spin−orbit level	NLF calc[a]	DCLF calc[b]	obs	NLF calc[a]	DCLF calc[b]	obs
$^3T_{2g}$	E	10 775	10 740	11 050	11 865	12 405	12 425
	T_1	10 940	10 955		12 315	12 325	
	T_2	11 225	11 290		12 590	12 650	
	A_2	11 355	11 445		12 725	12 810	
^1E_g	E	13 400	13 370	13 335	13 025	9 780	9 980
$^3T_{1g}(F)$	A_1	17 055	16 870	18 020	18 690	18 525	19 180
	T_1	17 400	17 275		19 050	18 370	
	T_2	17 890	17 805		19 445	18 715	
	E	18 010	17 970		19 530	18 800	
$^1A_{1g}$	A_1	22 570	22 325	22 450	21 870	16 830	16 515
$^3T_{1g}(P)$	E	28 290	28 090	28 570	30 140	29 755	30 135
	T_1	28 405	28 185		30 225	29 805	
	T_2	28 585	28 275		30 285	29 850	
	A_1	28 595	28 395		30 310	29 790	

[a] Energies calculated using the normal ligand-field model (NLF) based on the following parameter values. $[Ni(NH_3)_6]^{2+}$: $B = 850$, $C = 3450$, $10Dq = 11\,050$, $\zeta = 500$ cm^{-1}. $[Ni(AMN_3S_3sar)]^{2+}$: $B = 803$, $C = 3260$, $10Dq = 12\,425$, $\zeta = 500$ cm^{-1}. [b] Energies calculated using the differential covalency ligand-field model (DCLF) based on the following parameter values. $[Ni(NH_3)_6]^{2+}$: $f_t = 0.90$, $f_e = 0.87$, $10Dq = 11\,300$ cm^{-1}. $[Ni(AMN_3S_3sar)]^{2+}$: $f_t = 0.90$, $f_e = 0.75$, $10Dq = 13\,400$ cm^{-1}.

spin-allowed $^3A_{2g} \rightarrow {}^3T_{1g}(F)$ transitions in these complexes. In octahedral symmetry, the $^3T_{1g}(F)$ state comprises $A_1 + E + T_1 + T_2$ spin−orbit levels whereas the $^1A_{1g}$ state has only one spin−orbit level of A_1 symmetry. Thus, analogously to the $^1E_g - {}^3T_{2g}(E)$ spin−orbit interaction, the $^1A_{1g}$ state may mix with the A_1 spin−orbit component of the $^3T_{1g}(F)$ state. Evidence of this process is apparent in the spectra of the $[Ni(AMN_5Ssar)]^{2+}$, $[Ni(AMN_4S_2sar)]^{2+}$, and $[Ni(AMN_3S_3sar)]^{2+}$ complexes shown in Figure 2. Finally, in complexes with weaker donors, the smaller ligand field strength and larger Racah parameters can lead to overlap of the ^1E_g state with the $^3T_{1g}(F)$ state. In this case, the ^1E_g state can interact with the E spin−orbit component of the $^3T_{1g}(F)$ state. A detailed study of this phenomenon in the $[Ni(H_2O)_6]^{2+}$ complex was reported by Solomon and Ballhausen.[15]

Differential Nephelauxetic Effects. Although amine and thioether donors exert similar ligand-field strengths, they exhibit markedly different nephelauxetic effects due to the large differences in covalency of the Ni−N and Ni−S bonds. The increased metal−ligand covalency associated with the sulfur donor results in a reduction in interelectron repulsion, as evidenced by the dramatic shift to lower energy of the $^3A_{2g} \rightarrow {}^1E_g$ and $^3A_{2g} \rightarrow {}^1A_{1g}$ spin-forbidden transitions as the number of sulfur donors increases. The presence of significant metal−ligand covalency has implications when ligand-field parameters are determined on the basis of the best fit of calculated transition energies to the observed band positions. To illustrate this effect, the octahedral ligand-field parameters *B*, *C*, and $10Dq$ were determined for all five encapsulating complexes, on the basis of their low-temperature spectra, using the d^8 energy expressions previously reported.[1b] The best fit values of *B*, *C*, and $10Dq$ determined for each complex are listed in Table 5 and can be compared to those obtained for $[Ni(NH_3)_6]^{2+}$ (see Table 6) using the band positions reported for the low-temperature single-crystal spectrum.[16] In all cases, the spin-forbidden $^3A_{2g} \rightarrow {}^1A_{1g}$ transition was not included in the fitting process because it was only resolved in the spectra of the $[Ni(AMN_4S_2sar)]^{2+}$ and $[Ni(AMN_3S_3sar)]^{2+}$ complexes.

In the case of $[Ni(NH_3)_6]^{2+}$, very good agreement between calculated and observed transition energies is found for the parameter values $B = 850$, $C = 3450$, $10Dq = 11\,050$, and $\zeta = 500$ cm^{-1}, giving a C/B ratio of ∼4.0 (*cf.* free-ion ratio of 4.6). For $[Ni(diAMN_6sar)]^{2+}$, the C/B ratio has dropped slightly to ∼3.8 but is still reasonably close to that found for $[Ni(NH_3)_6]^{2+}$. However, in the remaining encapsulating complexes, a progressive reduction in the C/B ratio, down to 2.5 in the case of the $[Ni(Me_2S_6sar)]^{2+}$ complex, is observed with increasing number of sulfur donors. Furthermore, the calculated position of the $^3A_{2g} \rightarrow {}^1A_{1g}$ spin-forbidden transition in $[Ni(AMN_4S_2sar)]^{2+}$ and $[Ni(AMN_3S_3sar)]^{2+}$ is calculated over 1300 and 1600 cm^{-1} too high in energy, respectively, when the Racah *C* parameter is optimized to fit the $^3A_{2g} \rightarrow {}^1E_g$ transition. The unacceptably low C/B values and the poor calculated energies of the $^3A_{2g} \rightarrow {}^1A_{1g}$ transition are symptomatic of a significant differential nephelauxetic effect (originally termed differential radial expansion by Jørgensen[3]) arising from the covalency differences between the octahedral t_{2g} and e_g orbitals. Since the e_g orbitals are σ antibonding with respect to the ligands while the t_{2g} orbitals are nonbonding (neglecting any π donor/acceptor character of the thioether ligand), this differential nephelauxetic effect will increase with the number of sulfur donors around the nickel(II) ion.

It is possible to achieve some measure of the differential nephelauxetic effect by determining the Racah *B* parameter independently for the spin-allowed and spin-forbidden transitions. In the case of $[Ni(NH_3)_6]^{2+}$, values of $B = 850$ and 800 cm^{-1} are obtained for the spin-allowed and spin-forbidden transitions, respectively, when the C/B ratio is maintained at the free-ion ratio of 4.6. The 6% reduction in *B* indicates only a small differential nephelauxetic effect in this complex. In contrast, values of $B = 803$ and 565 cm^{-1} for the spin-allowed and spin-forbidden transitions, respectively, are found for $[Ni(AMN_3S_3sar)]^{2+}$. The 30% reduction in the Racah *B* parameter for the spin-forbidden transitions is indicative of a substantial differential nephelauxetic effect in this complex.

The failure of the normal octahedral ligand-field model to account for this differential covalency effect lies in the assumption that the same values of the Racah *B* and *C* interelectron repulsion parameters can be applied to all states, irrespective of the electron configuration involved. However, this assumption is not justified when significant metal−ligand covalency is present. For instance, both the ^1E_g and $^1A_{1g}$ states arise from the ground $(t_{2g})^6(e_g)^2$ configuration and thus the $^3A_{2g} \rightarrow {}^1E_g$ and $^3A_{2g} \rightarrow {}^1A_{1g}$ spin-forbidden transitions correspond to pure spin flips within the e_g orbitals. For these transitions, interelectron repulsion effects are confined to the e_g orbitals only. In contrast, both the $^3T_{2g}$ and $^3T_{1g}(F)$ states arise from the excited $(t_{2g})^5(e_g)^3$ configuration and involve interelectron repulsion effects over both the t_{2g} and e_g orbitals. Since the e_g orbitals experience greater metal−ligand covalency, interelectron repulsion effects are reduced in the e_g relative to the t_{2g} orbitals. The $^3A_{2g} \rightarrow {}^1E_g$ and $^3A_{2g} \rightarrow {}^1A_{1g}$ spin-forbidden transitions will therefore require lower values for the Racah *B* and *C* interelectron repulsion parameters than the spin-allowed transitions. In general, transitions arising from different electron configurations will require different Racah *B* and *C* interelectron repulsion parameters.

In the past, attempts to account for covalency differences have generally involved the use of the reduction parameters[17] β_{35}, β_{55}, and β_{33} with an analogous set associated with the Racah C parameter. However, these reduction parameters do not dis-

(15) Solomon, E. I.; Ballhausen, C. J. *Mol. Phys.* **1975**, *29*, 279.
(16) Schreiner, A. F.; Hamm, D. J. *Inorg. Chem.* **1973**, *12*, 2037.
(17) Lever, A. B. P. *Inorganic Electronic Spectroscopy*, 2nd ed.; Elsevier Press: New York, 1984.

Table 7. Exact Expressions for Selected d^8 Octahedral State Energies Using the Differential Covalency Ligand-Field Model

$$E(^3A_{2g} \rightarrow {}^1E_g) = 0.5Bf_t^2 + 10Dq + 8Bf_e^2 + C(f_e^2 + f_t^2) - \frac{\sqrt{(B^2f_t^2(48f_e^2 + f_t^2) - 4Bf_t^2(C(f_e^2 - f_t^2) - 10Dq) + 4C^2(f_e^4 - 2f_e^2f_t^2 + f_t^4) - 80CDq(f_e^2 + f_t^2) + 400Dq^2)}}{2}$$

$$E(^3A_{2g} \rightarrow {}^3T_{2g}) = -8Bf_ef_t + 10Dq + 8Bf_e^2$$

$$E(^3A_{2g} \rightarrow {}^3T_{1g}(F)) = B\left(2f_ef_t - \frac{5f_t^2}{2}\right) + 15Dq + 8Bf_e^2 - \frac{\sqrt{(B^2f_t^2(16f_e^2 + 184f_ef_t + 25f_t^2) - 20BDqf_t(4f_e + 5f_t) + 100Dq^2)}}{2}$$

$$E(^3A_{2g} \rightarrow {}^3T_{1g}(P)) = B\left(2f_ef_t - \frac{5f_t^2}{2}\right) + 15Dq + 8Bf_e^2 + \frac{\sqrt{(B^2f_t^2(16f_e^2 + 184f_ef_t + 25f_t^2) - 20BDqf_t(4f_e + 5f_t) + 100Dq^2)}}{2}$$

$$E(^3A_{2g} \rightarrow {}^1A_{1g}) = B(4f_e^2 + 5f_t^2) + C\left(2f_e^2 + \frac{5}{2}f_t^2\right) + 10Dq + 8Bf_e^2 - \frac{\sqrt{(4B^2(16f_e^4 - 16f_e^2f_t^2 + 25f_t^4) + 4B(C(16f_e^4 - 16f_e^2f_t^2 + 25f_t^4) - 20Dq(4f_e^2 - 5f_t^2)) + C^2(16f_e^4 - 16f_e^2f_t^2 + 25f_t^4) - 40CDq(4f_e^2 - 5f_t^2) + 400Dq^2)}}{2}$$

tinguish between the spin-allowed $^3T_{1g}(F)$ and $^3T_{1g}(P)$ transitions which correspond to one- and two-electron excitations to the e_g orbitals, respectively. In all, three different sets of Racah parameters are required to adequately model the observed spectral transitions arising from the three possible configurations $(t_{2g})^6(e_g)^2$, $(t_{2g})^5(e_g)^3$, and $(t_{2g})^4(e_g)^4$. Since at best only five d−d transitions are observed in the spectra of octahedral Ni(II) complexes, the independent fit of six different Racah interelectron repulsion parameters and the octahedral field parameter $10Dq$ is not possible, and so a less parametrized model must be sought.

The differential covalency ligand-field model[18] described by Lohr appears particularly attractive, as the whole interelectron repulsion problem for octahedral symmetry involves only two independent variables which take account of the covalency differences between the t_{2g} and e_g orbitals. In Lohr's model, it is assumed that the metal-based molecular orbitals are of the form

$$\Psi = c_d\phi_d + c_l\phi_l \qquad (c_d > c_l)$$

where c_d and c_l are the coefficients of the metal d and ligand atomic orbitals, ϕ_d and ϕ_l, respectively, and c_d is assumed to be much larger than c_l. If higher order terms are neglected, the reduction or covalency factors, f_d, for the metal d orbitals can be expressed as

$$f_d = c_d^2 + c_dc_lS_{dl}$$

where S_{dl} is the usual metal−ligand orbital overlap integral. For octahedral symmetry, only two covalency factors are necessary, designated f_t and f_e for the t_{2g} and e_g orbitals, respectively. These two covalency parameters will then reduce the matrix elements of all operators acting on the orbital part of the wave functions such as the interelectron repulsion and spin−orbit coupling operators.

The interelectron repulsion matrix elements for the d^8 configuration can be expressed in terms of two-electron integrals which are then reduced using the above covalency factors according to

$$\int \Psi_i^*(1)\,\Psi_j(1)\,\frac{e^2}{r_{12}}\,\Psi_k^*(2)\,\Psi_l(2)\,d\tau_1\,d\tau_2 = (\alpha A + \beta B + \gamma C)(f_if_jf_kf_l)^{1/2}$$

where α, β, and γ are whole numbers corresponding to the usual coefficients of the Racah parameters if pure 3d orbitals were involved. The f_i, f_j, f_k, and f_l parameters, which correspond to either f_t or f_e, are the appropriate covalency factors for the d orbitals ϕ_i, ϕ_j, ϕ_k, and ϕ_l involved in the molecular orbitals Ψ_i, Ψ_j, Ψ_k, and Ψ_l, respectively. In general, $f_e < f_t < 1$, with a smaller value implying greater metal−ligand covalency.

In Lohr's model, spin−orbit coupling was not considered but obviously is necessary in any reasonable analysis of the spectra of octahedral Ni(II) complexes. It can be easily incorporated by recognizing that the above covalency factors are also relevant in the matrix elements of the spin−orbit coupling operator if ligand centered spin−orbit coupling is ignored. These matrix elements can be expressed in one-electron form involving either the t_{2g} or e_g orbitals, for which the appropriate reduction expression is

$$\langle\Psi_i|\mathbf{H}_{so}|\Psi_j\rangle = \langle\phi_i|\zeta\mathbf{l}\cdot\mathbf{s}|\phi_j\rangle(f_if_j)^{1/2}$$

where again the f_i and f_j correspond to either f_t or f_e and ζ is the one-electron spin−orbit coupling parameter. To illustrate the use of these expressions, the off-diagonal matrix elements of the electrostatic, $\mathbf{H}_{el}$, and spin−orbit coupling, $\mathbf{H}_{so}$, operators involving the E spin−orbit levels of the $^3T_{1g}(F)$ and $^3T_{1g}(P)$ states are evaluated. From the electrostatic and spin−orbit matrices tabulated by Griffith,[19] one obtains

$$\langle(t_{2g})^5(e_g)^3\,{}^3T_{1g}(E)|\mathbf{H}_{el}|(t_{2g})^4(e_g)^4\,{}^3T_{1g}(E)\rangle = 6B$$

$$\langle(t_{2g})^5(e_g)^3\,{}^3T_{1g}(E)|\mathbf{H}_{so}|(t_{2g})^4(e_g)^4\,{}^3T_{1g}(E)\rangle = {}^1/_2\zeta$$

The electrostatic matrix element above can be expressed in terms of the two-electron matrix element $\langle t_{2g}(1)\,e_g(2)|\mathbf{e}^2/\mathbf{r}_{12}|t_{2g}(1)\,t_{2g}(2)\rangle$ and thus will involve a covalency factor of $(f_t^3f_e)^{1/2}$. The spin−orbit matrix element can be expressed in terms of the one-electron matrix element $\langle t_{2g}|\zeta\mathbf{l}\cdot\mathbf{s}|e_g\rangle$ and will involve a covalency factor of $(f_tf_e)^{1/2}$. The overall covalency-corrected off-diagonal matrix element will therefore take the form

$$\langle(t_{2g})^5(e_g)^3\,{}^3T_{1g}(E)|\mathbf{H}_{el} + \mathbf{H}_{so}|(t_{2g})^4(e_g)^4\,{}^3T_{1g}(E)\rangle = 6B(f_t^3f_e)^{1/2} + {}^1/_2\zeta(f_ef_t)^{1/2}$$

In the absence of spin−orbit coupling, exact expressions for the octahedral d^8 state energies, taking account of full configuration interaction, can be determined algebraically and are listed

(18) Lohr, L. L. *J. Chem. Phys.* **1966**, *45*, 3611.

(19) Griffith, J. S. *The Theory of Transition-Metal Ions*; Cambridge University Press: Cambridge, U.K., 1961.

in Table 7. If spin−orbit coupling is included, it is necessary to solve the secular determinant numerically. In order to do this, the d^8 octahedral basis functions were constructed as $|(t_{2g})^n(e_g)^m\ S\Gamma J\rangle$, where S is the spin state, Γ is the orbital symmetry, and J is the spin−orbit symmetry. The necessary electrostatic and spin−orbit coupling matrix elements were determined using the tables of Griffith.[19] The contribution of the Racah A parameter to the diagonal electrostatic terms is constant and can be avoided by subtracting the common factor $28A - 42B + 21C$. Cubic field terms of $10Dq$ and $20Dq$ were added to all diagonal matrix elements associated with the $(t_{2g})^5(e_g)^3$ and $(t_{2g})^4(e_g)^4$ configurations, respectively. Finally, the appropriate covalency factors were included in the electrostatic and spin−orbit coupling terms. The complete matrix was then block-diagonalized on the basis of spin−orbit symmetry for appropriate parameter values. The Racah B and C interelectron repulsion parameters and the one-electron spin−orbit coupling parameter ζ were maintained at the free-ion values for Ni(II) corresponding to $B = 1041$, $C = 4831$, and $\zeta = 649$ cm^{-1}.[17] The covalency factors f_t and f_e along with the ligand-field splitting parameter, $10Dq$, were adjusted to give the best fit to the observed band positions. Thus, in addition to accounting for differential covalency effects, the model has the further advantage in that it only requires three adjustable parameters compared to four (B, C, $10Dq$, and ζ) in the normal octahedral ligand-field model.

In order to compare the normal and differential covalency ligand-field models, calculations were performed to obtain the best fit of calculated energies to the observed d−d transitions in the complexes $[Ni(NH_3)_6]^{2+}$ and $[Ni(AMN_3S_3sar)]^{2+}$. The calculated and observed transition energies and best fit parameter values for both models are given in Table 6. In the case of $[Ni(NH_3)_6]^{2+}$, both models give comparable fits with the differences between observed and calculated energies (averaged over all spin−orbit components) less than 500 cm^{-1}. This is not surprising given that the f_e and f_t parameters are not too different, indicating that the t_{2g} and e_g orbitals experience similar metal−ligand covalency and thus differential nephelauxetic effects are relatively small. In contrast, whereas the calculated energies are within 500 cm^{-1} of the observed values for $[Ni(AMN_3S_3sar)]^{2+}$ using the differential covalency ligand-field model, they are out by as much as 5300 cm^{-1} when the normal ligand-field model is used with the C/B ratio maintained at the value of 4.06 found for $[Ni(NH_3)_6]^{2+}$. From Table 6 it is seen that there is now a significant difference between the f_t and f_e covalency parameters, indicating that the e_g orbitals are experiencing much greater metal−ligand covalency than the t_{2g} orbitals. The large difference between the f_t and f_e parameters highlights the extent of the differential nephelauxetic effect in $[Ni(AMN_3S_3sar)]^{2+}$ and thus explains the failure of the normal ligand-field model to reproduce the observed transition energies in this complex. In general, application of the differential covalency ligand-field model to the spectra of the Ni(II)-encapsulating complexes, as well as other octahedral Ni(II) complexes involving nitrogen and sulfur donors, resulted in substantially better fits to the observed positions of both spin-allowed and spin-forbidden transitions.

The best fit values of the f_t and f_e covalency parameters and $10Dq$ for the encapsulating and other Ni(II) complexes of interest are listed in Table 8. Whereas the f_t parameter remains fairly static around 0.9, the f_e parameter changes dramatically from 0.87−0.83 for N_6 complexes down to 0.69 for S_6 donor complexes. The negligible change observed in the f_t parameter is not surprising because the t_{2g} orbitals are essentially nonbonding in these complexes. Its deviation from unity can be largely attributed to the central-field covalency effect,[17] where the lone pairs of electrons on the donor ligands screen the d electrons from the nuclear charge, thereby dilating the d shell and reducing interelectron repulsion. In the first instance, this effect should result in a similar reduction in both f_t and f_e. Lohr, in his study of $MnCO_3$, found f_t to be closer to 0.95.[18] The higher value is consistent with the weaker ligand-field strength of oxygen donors which should reduce the central-field covalency effect compared to the nitrogen and sulfur donors used in our study. To check this effect in relation to Ni(II), we fitted the spectrum of $[Ni(H_2O)_6]^{2+}$, on the basis of the band positions reported for the low-temperature single-crystal spectra,[15] and obtained the parameter values $10Dq = 8500$, $f_t = 0.96$, and $f_e = 0.95$. Again, the f_t parameter is higher than that found for the encapsulating complexes with nitrogen and sulfur donors in agreement with Lohr's results. The progressive reduction observed in the f_e parameter as the number of sulfur donors increases is a direct reflection of the increased metal−ligand covalency for the e_g orbitals due to their σ antibonding character. In relation to the pure nitrogen donor complexes, the calculations clearly reveal the increased metal−ligand covalency associated with the macrocyclic and encapsulating ligands compared to the hexaammine complex.

Table 8. Differential Covalency Ligand-Field Model Parameters for Nickel(II) Complexes

nickel(II) complex		differential covalency parameters (cm^{-1})			
ligand	coordn	f_t	f_e	$10Dq$	$10(Dq - Dq^*)$[a]
NH_3	N_6	0.9	0.87	11 250	200
en	N_6	0.9	0.84	11 900	270
[9]aneN_3	N_6	0.9	0.83	13 200	300
diAMN_6sar	N_6	0.9	0.83	13 050	325
AMN_5Ssar	N_5S	0.9	0.80	13 000	560
[9]aneN_2S	N_4S_2	0.9	0.79	12 700	600
AMN_4S_2sar	N_4S_2	0.9	0.78	13 150	685
AMN_3S_3sar	N_3S_3	0.9	0.75	13 300	875
[9]aneS_2N	N_2S_4	0.9	0.74	13 150	950
[9]aneS_3	S_6	0.9	0.70	14 150	1100
Me_2S_6sar	S_6	0.9	0.69	14 800	1125

[a] Dq^* corresponds to the observed $^3A_{2g} \rightarrow {}^3T_{2g}$ transition energy.

Another point which emerges from the data given in Table 8 is that the value of $10Dq$ calculated using the differential covalency ligand-field model is always higher than the energy of the $^3A_{2g} \rightarrow {}^3T_{2g}$ spin-allowed transition which equates to $10Dq$ in the normal octahedral ligand-field model. This difference is seen to progressively increase with the number of sulfur donors. On the basis of the energy expressions given in Table 7, the energy of the $^3A_{2g} \rightarrow {}^3T_{2g}$ transition (ignoring spin−orbit coupling) is given by

$$E(^3A_{2g} \rightarrow {}^3T_{2g}) = 10Dq + 8B(f_e^2 - f_e f_t)$$

Consequently, when f_e is different from f_t, there exists a covalency correction to the energy of the $^3A_{2g} \rightarrow {}^3T_{2g}$ transition. The more covalent the donor ligand is, the greater the difference between f_e and f_t and thus the larger the discrepancy between the calculated $10Dq$ value and the $^3A_{2g} \rightarrow {}^3T_{2g}$ transition energy. The largest discrepancy, approximately 1100 cm^{-1}, occurs for the Ni(S_6) complexes. A comparison of the $10Dq$ values for Ni(N_6) and Ni(S_6) complexes in Table 8 reveals the surprising result that the thioether ligand actually exerts a ligand-field strength over 10% greater than that of amine donors. On the basis of these results, it is anticipated that other strongly covalent ligands, such as CN^-, Br^-, I^-, CO, and phosphorus donors, will also have significantly larger ligand-field strengths than

those derived simply from the energy of the $^3A_{2g} \rightarrow {}^3T_{2g}$ spin-allowed transition.

Conclusions

The encapsulating complexes of Ni(II) comprising mixed nitrogen and sulfur donors provide a particularly useful series to study the influence of spin−orbit mixing and differential nephelauxetic effects on the electronic spectra of octahedral Ni(II) complexes because the nitrogen/sulfur donor ratio can be systematically altered without significantly affecting the macrocyclic backbone structure. The additional advantage of the nitrogen and thioether donors exerting comparable ligand-field strengths but dramatically different nephelauxetic effects makes possible substantial changes in the spectra as the donor set around the Ni(II) ion is varied. The anomalous band shapes observed for the spin-allowed $^3A_{2g} \rightarrow {}^3T_{2g}$ transition can be attributed to spin−orbit-induced mixing between the E spin−orbit components of the ^1E_g and $^3T_{2g}$ states. As the number of sulfur donors increases, the spin-forbidden $^3A_{2g} \rightarrow {}^1E_g$ and $^3A_{2g} \rightarrow {}^1A_{1g}$ transitions undergo a dramatic shift to lower energy, indicative of a significant differential nephelauxetic effect arising from the covalency differences between the t_{2g} and e_g orbitals. As a consequence, no single set of Racah *B* and *C* interelectron repulsion parameters will adequately fit the observed spectra. By adapting Lohr's differential covalency ligand-field model to octahedral Ni(II) complexes and incorporating spin−orbit coupling effects, one can account for the covalency differences between the t_{2g} and e_g orbitals. On the basis of this model, the spectral transitions can be successfully reproduced using only three independent variables corresponding to the cubic field splitting parameter $10Dq$ and the covalency parameters f_t and f_e, associated with the t_{2g} and e_g orbitals, respectively. The relatively small reduction in f_t from unity is largely attributed to central-field covalency effects whereas the dramatic drop in f_e with an increasing number of sulfur donors is a direct consequence of the increased metal−ligand covalency associated with the thioether donor. Covalency differences between the t_{2g} and e_g orbitals also result in larger $10Dq$ values than those obtained simply from the energy of the $^3A_{2g} \rightarrow {}^3T_{2g}$ spin-allowed transition. This model should be applicable not only to other Ni(II) complexes involving covalent ligands, such as CN^-, CO, I^-, and phosphorus donors, but also to complexes containing transition metal ions other than Ni(II).

Acknowledgment. Professor A. Sargeson and Dr. P. Osvath are thanked for providing a sample of $[Ni(Me_2S_6sar)]^{2+}$ and Dr. L. Dubicki is thanked for fruitful discussions related to the differential nephelauxetic effect in Ni(II) complexes.

Supporting Information Available: Listings of anisotropic thermal parameters (Table S1), hydrogen positional and istropic thermal parameters (Table S2), torsional and conformation angles (Table S3), and intermolecular distances (Table S4) (13 pages). Ordering information is given on any current masthead page.

IC9614531